Transient Multi-Physics Modeling and Performance Degradation Evaluation of Direct Internal Reforming Solid Oxide Fuel Cell Focusing on Carbon Deposition Effect

Zheng Li, Guogang Yang *, Qiuwan Shen, Shian Li, Hao Wang, Jiadong Liao, Ziheng Jiang and Guoling Zhang

Marine Engineering College, Dalian Maritime University, Dalian 116026, China
* Correspondence: yanggg@dlmu.edu.cn

Abstract: The performance degradation issue caused by carbon deposition has limited the commercial application of natural-gas-fueled solid oxide fuel cells. Most previous corresponding studies are based on thermodynamic equilibrium analyses, while long-term transient evaluation work is lacking. Therefore, a transient multi-physics numerical model is developed in present work. The corresponding long-term performance degradation evaluation is then conducted. The results show that, for a direct internal reforming solid oxide fuel cell, the increase in carbon deposition and deterioration of performance degradation were concentrated in the first 180 days of steady−state operation and slowed down at the later stage. The electrode inlet rapidly developed a high concentration of carbon deposition after 180 days of steady−state operation. The deposited carbon deteriorated the gas transport and decayed reaction activity within the porous electrode, eventually inducing a deactivation zone with 0 current density at the inlet. Key measures to inhibit carbon deposition should be implemented within the first 180 days of operation, and the pre-reformed operation of natural gas is encouraged for natural-gas-fueled solid oxide fuel cells.

Keywords: solid oxide fuel cell; carbon deposition effect; transient multi-physics modeling; long-term performance evaluation

1. Introduction

As a pillar of global trade, the maritime industry provides key support for the development of the world economy, but it also brings serious pollution emissions. According to the emission reduction roadmap proposed by the IMO (International Maritime Organization), the maritime industry needs to achieve more than a 50% carbon emission reduction by 2050 compared to the level of 2008 [1]. In the face of increasingly stringent emission regulations, it is becoming more difficult for traditional internal combustion engines to meet the requirements of energy use [2], while electric propulsion plants are enjoying a renaissance. Due to their high power density, high thermal efficiency, and convenience to adapt to marine natural gas fuel with existing fire-fighting measures, solid oxide fuel cells are considered one of the most promising directions for new energy vessels [3].

Nonetheless, the performance degradation issue of natural-gas-fueled solid oxide fuel cells caused by carbon deposition during long-term operation limits their marine application, which inspires further research. In the open literature, there are two different approaches to solving this problem. One is to develop new catalysts to inhibit carbon deposition based on the elucidation of the carbon deposition mechanism. For example, decorative fluorite or peroxidation could be adopted to enhance the coking resistance of Ni/YSZ electrodes by increasing the flux of oxygen ions and accelerating the fuel cell reaction [4,5]. Similarly, the decoration of perovskite with nano-sized exsolved metallic particles could also be adopted to enhance the coking resistance of Ni/YSZ electrodes by slowing down the generation of carbon fibers [6]. In addition, decorating alkaline earth

metal oxides could be adopted to speed up the removal of carbon and enhance the coking resistance of Ni/YSZ electrodes [7]. Rabuni et al. [8] incorporated a copper-ceria layer inside the micro-channels of an anode scaffold and experimentally demonstrated their stability resistance to carbon deposition. Zhao et al. [9] explored the effect of Ni-Mo catalyst layers on inhibiting carbon deposition in Ni-YSZ anodes. Zhang et al. [10] elucidated the carbon-resistant mechanism of Ni-Fe alloy catalysts in a solid oxide fuel cell. Similar studies can also be found in Refs. [11–13]. The development of new catalysts has positive implications for improving resistance to carbon deposition and extending the lifetimes of solid oxide fuel cells, but further research is needed to confirm their commercial viability. For example, most of the new catalysts face problems of extra costs. The catalytic activity of copper-based catalysts differs significantly from that of nickel-based catalysts when natural gas is fueled [14]. Additionally, the reaction of alkaline earth metal oxides under high temperatures and CO_2 operating conditions could distort electrode structure [15]. Moreover, the thermomechanical compatibility of new electrode materials with other cell components still needs further confirmation, which is extremely important for the long-term performance and commercialization of solid oxide fuel cells.

Taking implementation ability, durability, reliability, and cost into account, another more practical approach is to conduct online monitoring of the state of carbon deposition and corresponding long-term degradation performance evaluations of solid oxide fuel cells. Based on this, we can identify potential degradation changes as early as possible and, thus, adopt appropriate optimization strategies to monitor the health of solid oxide fuel cells and regulate them online to avoid degradation. With regard to appropriate optimization strategies, corresponding experiments and related kinetic studies provide a key foundation. Yurkiv [16] reviewed the available literature and pointed out that carbon deposition could be controlled optimally by operating temperature, fuel composition, polarization state, and exposure type. Kirtley et al. [17] examined rates of carbon formation and removal from Ni/YSZ cermet anodes by adjusting the oxygen-to-carbon molar ratio of supply fuel during in situ operation. They compared the effects of H_2O, O_2, and CO_2 on the removal of carbon deposits. The corresponding results showed that the introduction of H_2O was the most effective in removing carbon deposits, while the introduction of CO_2 was the least effective. Schluckner et al. [18] demonstrated that carbon deposition within solid oxide fuel cells was closely related to both the operating temperature and fuel composition, which determined the form of deposited carbon. Their results indicated that carbon deposition in the fibrous form began at around 400 °C, peaked at around 700 °C, and was dominated by the cracking reaction of methane. Carbon deposition in the graphite form began at much lower temperatures, peaked at around 550 °C, then decreased with increasing temperature, and was dominated by carbon-monoxide-induced carbon deposition. According to the form and cause of the deposited carbon, some other researchers [19,20] have further demonstrated the effects of H_2O, H_2, and CO_2 on carbon removal from solid oxide fuel cells.

As for the performance deterioration caused by inhibiting carbon deposition only by adjusting fuel composition and temperature [17], many researchers have also conducted further research. For example, Subotic et al. [21] demonstrated a method to simultaneously remove carbon and recover the initial electrochemical performance. They first generated carbon in load mode and then demonstrated that combining load mode adjustment and hydrogen or steam addition could remove carbon while recovering the electrochemical performance of a solid oxide fuel cell. The recovery time was only about 200 s when carbon dioxide was used, making it more realistic and feasible [22]. In addition, Han et al. [23] demonstrated that the use of oxygen ions supplemented with the addition of hydrogen to prevent the reoxidation of metallic nickel was effective for carbon removal. Similar results were also seen in the study of Reeping et al. [24]. The above literature provides detailed appropriate optimization strategies by adjusting operating conditions to deal with carbon deposition.
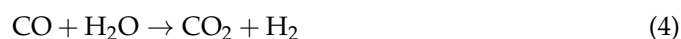
However, with regard to the online monitoring of the state of carbon deposition and corresponding long-term degradation performance evaluations of solid oxide fuel cells, there is rather limited research in the open literature. This is because the high operating temperatures and tight sealing requirements of solid oxide fuel cells make the in−situ measurement of temperature and carbon deposition a recognized challenge. As a result, the construction of a corresponding numerical model seems particularly important. Studies in the literature dealing with long-term performance degradation have only started to appear in recent years. For example, Yan et al. [24] evaluated the effect of change in porosity caused by carbon deposition on the performance of solid oxide fuel cells. Ma et al. [25] further evaluated the long-term performance of solid oxide fuel cells considering the unsteady state variation in porosity caused by carbon deposition. Zhang et al. [26] conducted a long-term performance evaluation of coal gasification syngas-fueled solid oxide fuel cells. Zhu et al. [27] conducted a corresponding evaluation of biomass-gas-fueled solid oxide fuel cells. These studies have evaluated the long-term performances of solid oxide fuel cells over an operating time of around 200 days and provide a valuable basis for further research.

In the present work, we further develop a transient multi-physics numerical model and conduct a long-term performance evaluation of a direct internal reforming solid oxide fuel cell during 20,000 h of operation. To the best of our knowledge, this is the first 20,000 h long-term performance evaluation for a direct internal reforming solid oxide fuel cell considering carbon deposition as of the work submission date. The corresponding evaluation results may lead to new findings and provide a design reference for solid oxide fuel cells in more demanding marine or power plant applications.

2. Physical Model and Numerical Method

2.1. Working Mechanism and Computational Domain Description

For a direct internal reforming natural-gas-fueled solid oxide fuel cell, in addition to electrochemical reactions, a methane steam reforming reaction, and a water–gas shift reaction, the thorny problem of carbon deposition has to be considered. According to the open literature, it is generally accepted that carbon deposition is mainly caused by a methane decomposition reaction (Equation (5)) and a Boudouard reaction (Equation (6)). Therefore, as shown in Equations (1)–(6), the following reactions occurring simultaneously within solid oxide fuel cells were considered:

$$1/2O_2 + 2e^- \rightarrow O^{2-} \tag{1}$$

$$H_2 + O^{2-} \rightarrow H_2O + 2e^- \tag{2}$$

$$CH_4 + H_2O \rightarrow CO + 3H_2 \tag{3}$$

$$CO + H_2O \rightarrow CO_2 + H_2 \tag{4}$$

$$CH_4 \rightarrow C(s) + 2H_2 \tag{5}$$

$$2CO \rightarrow C(s) + CO_2 \tag{6}$$

For the chosen computational domain, the half single cell shown in Figure 1 was used. Although single cells are stacked to form a stack for sufficient power in engineering use and there have been some stack-level simulation studies in the open literature [28–30], stack-level simulations have drawbacks in terms of high computing resource requirements and long computation times. In our study, as shown in Figure 1, single cells were stacked neatly to form a stack, and the whole stack could be approximated as the repeated operation of several single cells by imposing symmetry conditions. Therefore, half of a single cell was used as the final computational domain in the present work.
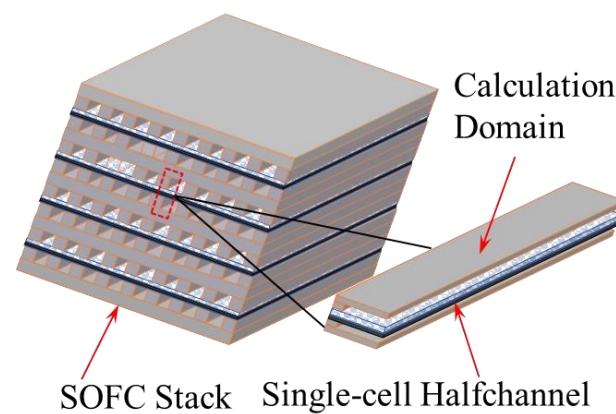
Figure 1. Schematic diagram of solid oxide fuel cell stack and calculation domain in the present work.

The detailed geometry parameters of the computational domain are shown in Table 1.

Table 1. Geometry parameters of the computational domain.

	Symbols	Values (mm)
Cell length	L	100
Cell width	W	1.5
Gas channel width	W_g	1
Interconnect height	h_i	1.15
Gas channel height	h_g	1
Anode support layer thickness	h_{as}	0.4
Anode function layer thickness	h_{af}	0.015
Electrolyte layer thickness	h_e	0.01
Cathode function layer thickness	h_{af}	0.02
Cathode support layer thickness	h_{af}	0.05

2.2. Basic Assumption

To ensure the validity and accuracy of the calculations, it should be highlighted that this work was carried out based on the following basic assumptions.

(1) The gas flow within the fuel cell remained laminar based on the reality of the low flow rate supply of the fuel channel.

(2) The gas mixture was considered a compressible ideal gas based on the facts of the high-temperature and low-pressure operating conditions.

(3) The fuel cell material was treated as continuous and isotropic.

(4) The active sites involved in the thermochemical and electrochemical reactions were uniformly distributed within the catalytic layer.

(5) Small amounts of extraneous gases in the fuel gas were ignored, e.g., the proportion of air was treated as 79% N_2 and 21% O_2, and natural gas was treated as 100% CH_4.

2.3. Governing Equations

2.3.1. Electrochemical Reaction and Thermochemical Reaction

The Butler–Volmer equation is one of the most widely used expressions to describe the relationship between activation overpotential and current density and was also used in the present work to calculate the local current density of the solid oxide fuel cell. It was calculated as follows:

$$i_v = \text{ASA} \cdot i_0 \left[\exp\left(\frac{\alpha n F}{RT} \eta_{act}\right) - \exp\left(-\frac{(1-\alpha)nF}{RT} \eta_{act}\right) \right] \tag{7}$$

where i_v is the current density in a specific volume, i_0 is the exchange current density, ASA is the active specific area, T is the local temperature, and η_{act} is the activation overpoten-

tial. The corresponding calculation method for exchange current density and activation overpotential can be found in our previous work [31].

For the thermochemical reaction shown in Equations (3) and (4), the corresponding reaction rate was computed as follows:

$$r_{MSR} = 63.6T^2 \exp(\frac{-27063}{T})c_{CH_4}c_{H_2O} - 3.7 \times 10^{-14}T^4 \exp(\frac{-232.78}{T})c_{CO}c_{H_2}^3 \tag{8}$$

$$r_{WGSR} = 1199T^2 \exp(\frac{-12509}{T})c_{CO}c_{H_2O} - 6.77 \times 10^4 T^2 \exp(\frac{-16909}{T})c_{CO_2}c_{H_2} \tag{9}$$

where r is the reaction rate, and c is the mole concentration of species.

For the methane decomposition reaction and the Boudouard reaction shown in Equations (5) and (6), respectively, the corresponding reaction rate was computed as follows [20,32]:

$$r_{MD} = \alpha \left(k_{MD} \left(p_{CH_4} - p_{H_2}^2 / K_{MD} \right) / \left(M_C \cdot (1 + k_H p_{H_2}^{0.5})^2 \right) \right) \tag{10}$$

$$r_{BR} = \alpha k_{BR} K_{CO} \frac{p_{CO} - p_{CO_2}/K_{BR}p_{CO}}{M_C(1 + K_{CO}p_{CO} + p_{CO_2}/K_{CO_2}K_{CO}p_{CO})^2} \tag{11}$$

where α is the reaction activity coefficient, k is the reaction rate constant, K is the equilibrium constant, p is the local pressure, and M_C is the molar mass of carbon.

The resulting deposited carbon concentration was computed as follows:

$$r_C = \frac{dC_C}{dt} = r_{MD} + r_{BR} \tag{12}$$

where t is the operation time, and C_C is the concentration of deposited carbon.

The attenuation of the reaction activity caused by carbon deposition was expressed as follows [32]:

$$\frac{d\alpha}{dt} = -\alpha k_a r_C^2 C_C \tag{13}$$

The attenuation of the porous electrode porosity caused by carbon deposition was expressed as follows:

$$\frac{d\varepsilon}{dt} = \frac{\varepsilon r_C M_C}{\rho_C} \tag{14}$$

The resulting attenuation of the porous electrode permeability was computed as follows:

$$\kappa = \kappa_0 \left(\frac{\varepsilon}{\varepsilon_0} \right)^{3.35} \tag{15}$$

where ε is the porosity of the porous electrode, κ is the permeability of the porous electrode, and the subscript 0 represents the original state.

2.3.2. Ion and Charge Transport

The ion and electron transport process within a solid oxide fuel cell can be expressed according to Ohm's law. It was expressed as follows:

$$i_e = \sigma_{eff,e} \nabla \varphi_e \tag{16}$$

$$i_i = \sigma_{eff,i} \nabla] \varphi_i \tag{17}$$

where φ is the potential, and the subscript e represents electron while i represents ion. σ_{eff} is the effective ion or electron conductivity rate, which was computed as follows:

$$\sigma_{eff,e,a} = \sigma_{Ni} \frac{V_{Ni,a}}{\tau_{e,a}} \tag{18}$$

$$\sigma_{\text{eff,i,a}} = \sigma_{\text{YSZ}} \frac{V_{\text{YSZ,a}}}{\tau_{\text{i,a}}} \tag{19}$$

$$\sigma_{\text{eff,e,c}} = \sigma_{\text{LSM}} \frac{V_{\text{LSM,c}}}{\tau_{\text{e,c}}} \tag{20}$$

$$\sigma_{\text{eff,i,c}} = \sigma_{\text{YSZ}} \frac{V_{\text{YSZ,c}}}{\tau_{\text{i,c}}} \tag{21}$$

$$\sigma_{\text{Ni}} = \frac{9.5 \times 10^7}{T} \exp\left(\frac{-1150}{T}\right) \tag{22}$$

$$\sigma_{\text{YSZ}} = 3.34 \times 10^4 \exp\left(\frac{-10300}{T}\right) \tag{23}$$

$$\sigma_{\text{LSM}} = \frac{4.2 \times 10^7}{T} \exp\left(\frac{-1200}{T}\right) \tag{24}$$

where V is the volume fraction, τ is the tortuosity, and the subscript a represents anode while c represents cathode.

2.3.3. Mass and Momentum Transport

Gas transport simultaneously occurs in the gas channel and porous electrode. Thus, the corresponding mass and momentum transport needed to be described separately.

For the gas channel, it was expressed as follows:

$$\frac{\partial \rho}{\partial t} + \nabla\left(\rho \vec{u}\right) = 0 \tag{25}$$

$$\frac{\partial\left(\rho \vec{u}\right)}{\partial t} + \nabla\cdot\left(\rho \vec{u}\vec{u}\right) = -\nabla p + \nabla\cdot\left[\mu(\nabla\vec{u} + \nabla\vec{u}^T) - \frac{2\mu}{3}\left(\nabla\cdot\vec{u}\right)\right] \tag{26}$$

For the porous electrode, it was expressed as follows:

$$\frac{\partial(\varepsilon\rho)}{\partial t} + \nabla\left(\rho \vec{u}\right) = Q_s \tag{27}$$

$$\frac{\partial\left(\rho \vec{u}/\varepsilon\right)}{\partial t} + \nabla\left(\frac{\rho \vec{u}\vec{u}}{\varepsilon}\right) = -\varepsilon\nabla p + \nabla\left[\mu(\nabla\vec{u} + \nabla\vec{u}^T) - \frac{2\mu}{3}\left(\nabla\vec{u}\right)\right] - \varepsilon\frac{\mu}{\kappa}\vec{u} \tag{28}$$

where Q_s is the mass source caused by the reaction, p represents the local pressure, and μ is the dynamic viscosity.

2.3.4. Heat and Species Transport

The heat transfer within the solid oxide fuel cell was simulated based on the local thermodynamic equilibrium method, which meant that the temperature difference between the gas phase and the solid phase in the electrode was negligible. It could be expressed as follows:

$$\frac{\partial\left(\rho c_p T\right)}{\partial t} + \rho\cdot c_p\cdot\vec{u}\cdot\nabla T - \nabla\cdot(k_{\text{eff}}\nabla T) = Q_h \tag{29}$$

where k_{eff} represents the effective thermal conductivity, and c_p represents the specific heat capacity. Q_h is the heat source term caused by the reaction, which was expressed as follows:

$$Q_h = Q_{ir} + Q_{re} + Q_r \tag{30}$$

where Q_{ir} is the irreversible heat source term during operation, Q_{re} is the electrochemical reaction heat source term, and Q_r is the thermochemical reaction heat term. The detailed calculation method can also be found in our previous work [31].

The species transport within the solid oxide fuel cell could be described by the convection–diffusion conservation equation. It could be expressed as follows:

$$\frac{\partial(\rho\varepsilon\omega_i)}{\partial t} + \nabla\left(\rho\omega_i\vec{u}\right) - \nabla\left\{\rho\omega_i\sum D_{\text{eff}}\left[\nabla x_i + \frac{1}{p}[(x_i - \omega_i)\nabla p]\right]\right\} = R_i \tag{31}$$

where, ω_i represents the mass fraction of ith component, and x_i represents its molar fraction. D_{eff} represents the effective diffusion coefficient, and R_i represents the corresponding mass source caused by varied reactions.

3. Solution Method and Model Validation

A numerical solution requires appropriate boundary conditions to describe the operating state of a solid oxide fuel cell. In the present work, Dirichlet boundary conditions were used for the gas inlet, while Neumann boundary conditions were used for the outlet. The right-side surface of the calculation domain was applied as the symmetry boundary, while the remaining external surfaces were insulation boundaries. More detailed boundary conditions are shown in Table 2, wherein T_0 is the inlet temperature with a value of 1073 K, p_0 is atmospheric pressure, the operating voltage V_{cell} is 0.7 V, the anode inlet velocity u_0 is 0.3 m/s, and the cathode is 0.75 m/s. According to the typical engineering conditions for direct internal reforming solid oxide fuel cells [33,34], the inlet fuel was a mixture of methane and steam with a molar ratio of 2.5.

Table 2. The boundary conditions of the simulation model in the present work.

Boundary Surface	Conditions
Inlet condition	$u_y = u_0, u_x = u_z = 0, T = T_0, \omega = \omega_{i,0}$
Outlet condition	$p = p_0, \nabla T = 0, \nabla\omega = 0$
Top surface condition	$\nabla u = 0, \nabla T = 0, \nabla\omega = 0, \nabla i = 0$
External surface of the anode-side interconnector	$\phi = 0, \nabla T = 0$
External surface of the cathode-side interconnector	$\phi = V_{\text{cell}}, \nabla T = 0$
Remaining external surfaces	$\nabla T = 0, \nabla i = 0$

For the research content of this paper, the model validation work needed to focus on two aspects: the first was the accuracy of the carbon deposition kinetic model, which was the basic guarantee for the long-term performance evaluation considering the carbon deposition effect; the other was the validation of the solid oxide fuel cell model. For rationality of the carbon deposition reaction kinetics model, the simulation results were compared with the experimental measured data from Zavarukhin et al. [32]. As shown in Figure 2, the comparison between the experimental data and the simulation results showed an overall satisfactory agreement. As for the validation of the solid oxide fuel cell model, the simulation results were also compared with experimental data by Hsieh et al. [35], which were also discussed in our previous work [31]. Based on the above comparisons, the rationality of the transient multi-physics numerical simulation in the present work could be confirmed.
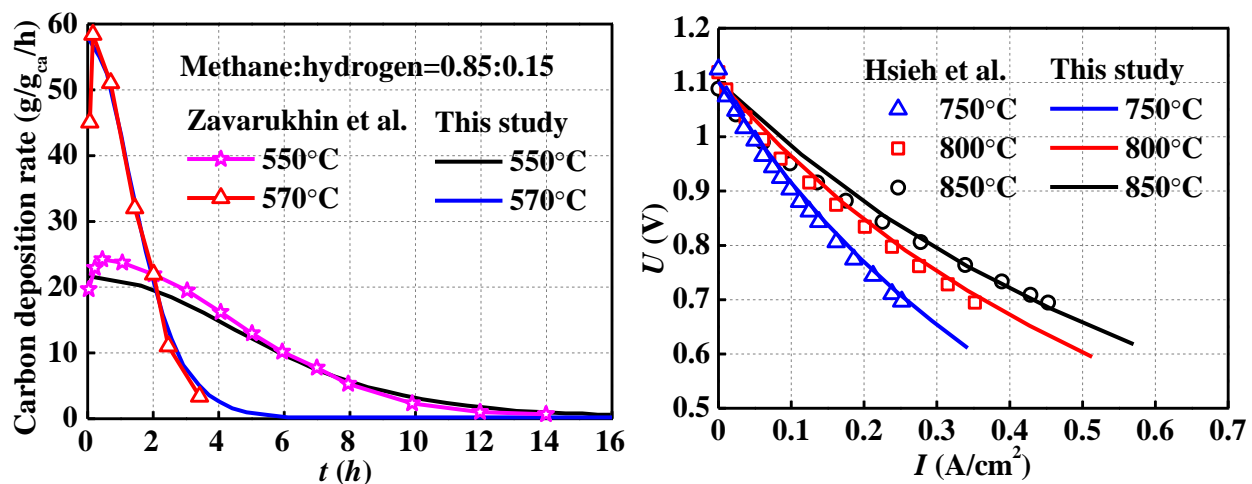
Figure 2. Comparison of simulated and experimental carbon deposition rates and polarization curves for SOFCs under different temperatures and pressure of 1 atm with data from Refs. [32,35].

4. Results and Discussions

Before conducting the discussion, it should be noted that the typical inlet fuel conditions for direct internal reforming solid oxide fuel cells [33,34], a mixture of methane and steam with a molar ratio of 2.5, were adopted in the present work. Although increasing the molar ratio may improve the carbon deposition within solid oxide fuel cells, it is outside the scope of this paper, as that is not a typical engineering condition. As previously mentioned, during long-term operation, carbon deposition inevitably occurs within direct internal reforming natural-gas-fueled solid oxide fuel cells. When a solid oxide fuel cell operates for a short time, the effect of carbon deposition on the porous electrode can be neglected. With an increase in operation time, carbon deposition has a non-negligible effect on long-term performance [20].

In general, the corresponding effects on the long-term performances of solid oxide fuel cells can be summarized into two main aspects [23,24]: (1) the effect on the microscopic morphology and transport properties of the porous electrode and (2) the effect on the reaction activity and the resulting output performance degradation. Therefore, the discussion is divided into three sections. The first section clarifies the spatial-temporal evolution of carbon deposition within the SOFC porous electrode during 20,000 h of steady−state operation. The resulting variation in porous electrode microscopic morphology and transport properties is discussed in the second section, while the variation in the reaction activity and current density are discussed in the third section.
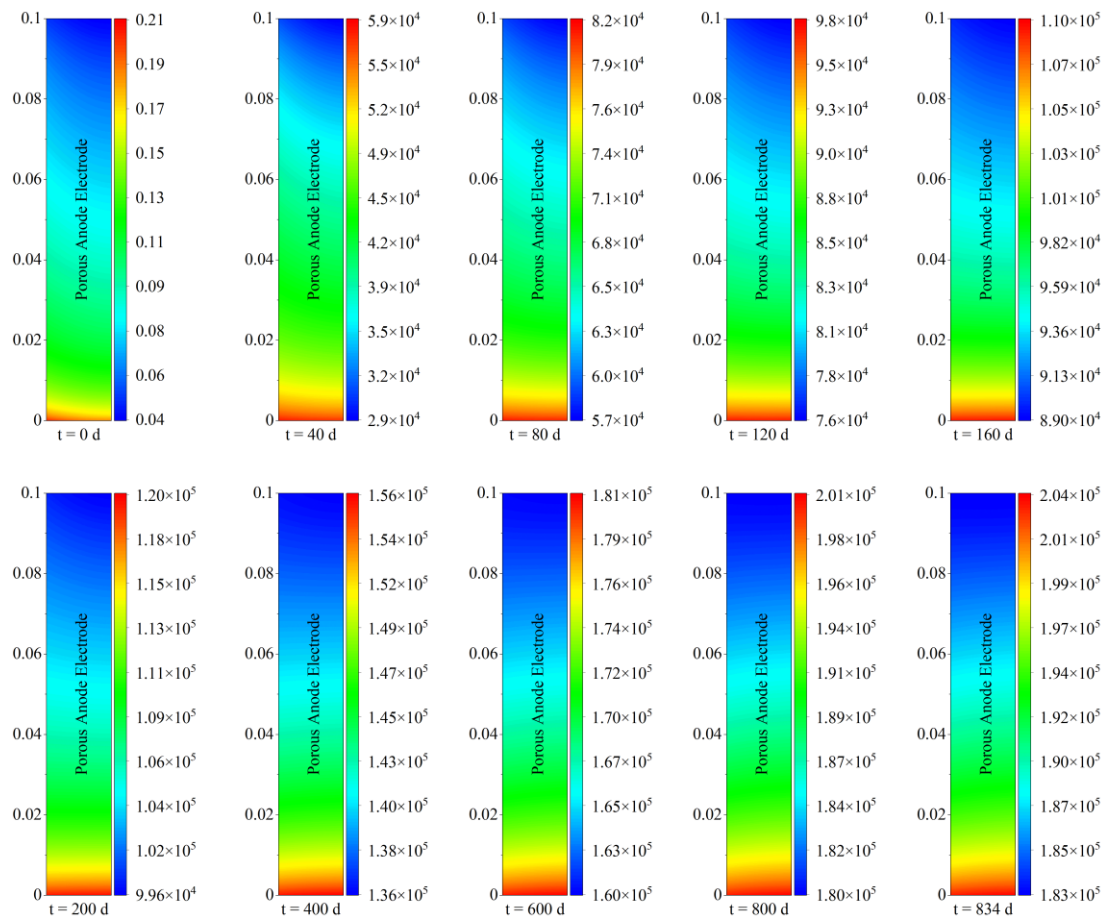
4.1. The Spatial-Temporal Evolution of Carbon Deposition

As previously mentioned, carbon deposition inevitably occurs within direct internal reforming natural-gas-fueled solid oxide fuel cells during long-term operation. When a solid oxide fuel cell operates for a short time, the effect of carbon deposition on the porous electrode can be neglected, while it has a non-negligible effect on the long-term performance of a solid oxide fuel cell with the increase in operation time. Therefore, the spatial-temporal evolution of carbon deposition within an SOFC porous electrode during long-term operation is the basis for the performance degradation evaluation of solid oxide fuel cells.

The spatial distribution of carbon deposition within the porous anode electrode under different operating periods is given in Figure 3. It is worth noting that the comparison between different running times needed to be differentiated by their respective legends. As can be seen from Figure 3, with regard to spatial distribution characteristics, carbon deposition near the inlet of the solid oxide fuel cell was more serious than that near the outlet, and carbon deposition near the left fuel channel was also more serious than that near the right electrolyte, which is similar to the results of Wang [24]. Taking the carbon

deposition condition after steady−state operation for 40 days as an example, the deposited carbon concentration near the porous electrode outlet was around 29,000 mol/m^3, while near the inlet, it was as high as 59,000 mol/m^3. This means that the deposited carbon concentration within the porous electrode was extremely uneven. It differed by half after 40 days of steady−state operation.

Figure 3. The spatial and temporal evolution of deposited carbon (mol/m^3) within the porous anode electrode of the solid oxide fuel cell during 20,000 h of steady−state operation.

With regard to temporal evolution characteristics, carbon deposition increased continually with the increase in operation time during 20,000 h of steady−state operation. More specifically, taking the carbon deposition concentration near the inlet as an example, it increased from 0.21 mol/m^3 to 5.9×10^4 mol/m^3 after operation for 40 days. During the subsequent period from 40 days to 160 days of operation, the corresponding carbon concentration further increased to a maximum of 1.1×10^5 mol/m^3. With the increase in operation time, carbon deposition continued to increase. Eventually, the continuous carbon deposition formed a high concentration value of 2.04×10^5 mol/m^3, which had a non-negligible effect on electrode porous structure and transport properties, causing a more deteriorated operation condition. It should be noted that the higher carbon deposition near the left inlet fuel channel was caused by the higher methane concentration at the inlet of the solid oxide fuel cell, which reflected the poor long-term performance of the direct internal reforming operation. Moreover, the highest value of carbon deposition concentration reached 2.04×10^5 mol/m^3, which indicated that the deposited carbon could be in the dense form of film carbon after 20,000 h of operation [16]. At this period, carbon deposition may be difficult to remove, and key measures to inhibit carbon deposition should be implemented early.

In order to describe the evolution trend of carbon deposition concentration under varied operating times more clearly, Figure 4 also demonstrates the detected values of local carbon deposition concentration at the electrode midpoint based on Figure 3. As shown in Figure 4, the 20,000 h performance evaluation captured the trend that carbon deposition increased rapidly at first and slowed down at later stages. During the steady−state operation period from 0 days to 180 days, the carbon deposition reached 1×10^5 mol/m^3 after 180 days of steady−state operation, with an average growth rate of around 556 mol/m^3/d. As for the operation period from 180 days to 360 days, the carbon deposition eventually reached 1.35×10^5 mol/m^3, with an average growth rate of around 194 mol/m^3/d. A further decreased growth rate was found with the increase in operation time. Overall, the growth rate (the line slope) of carbon deposition was greater around the first 180 days (around 4000 h) of steady−state operation. It could be inferred that high-speed carbon deposition mainly occurred in the early stage of 180 days (around 4000 h) of operation. Additionally, the carbon deposition rate gradually decreased with the increase in operation time. This indicated that key measures to inhibit carbon deposition can be placed in the early stage around 4000 h of solid oxide fuel cell operation.
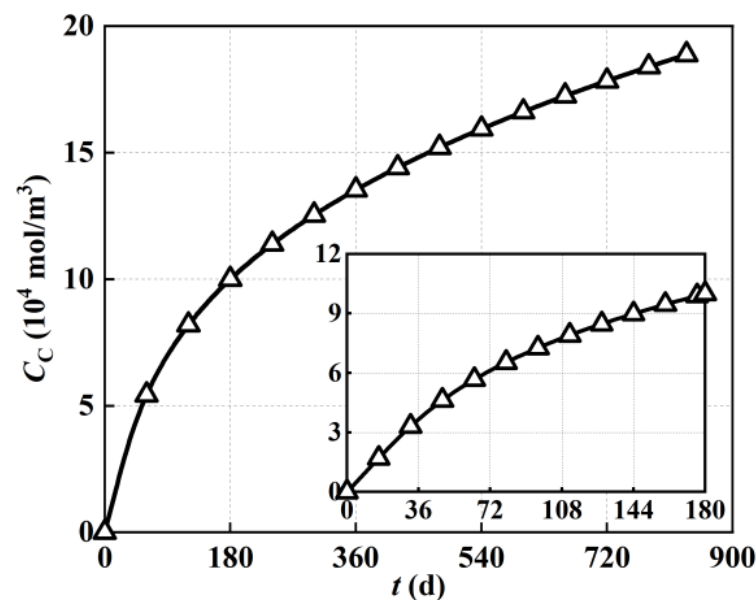
Figure 4. Variation in carbon deposition of porous anode electrode over operating time during 20,000 h of steady−state operation.

4.2. The Effect of Carbon Deposition on Microscopic Morphology and Transport Capacity of Porous Electrode

Deposited carbon adsorbs onto the solid surface of the porous electrode and occupies its void volume, causing changes in its microscopic morphology and the resulting deterioration in transport properties. Due to the occupancy of the void volume by deposited carbon, the porosity of the porous electrode is the first to be affected. Therefore, Figure 5 shows the spatial and temporal evolution of porosity within the porous anode electrode of the solid oxide fuel cell considering the carbon deposition effect.
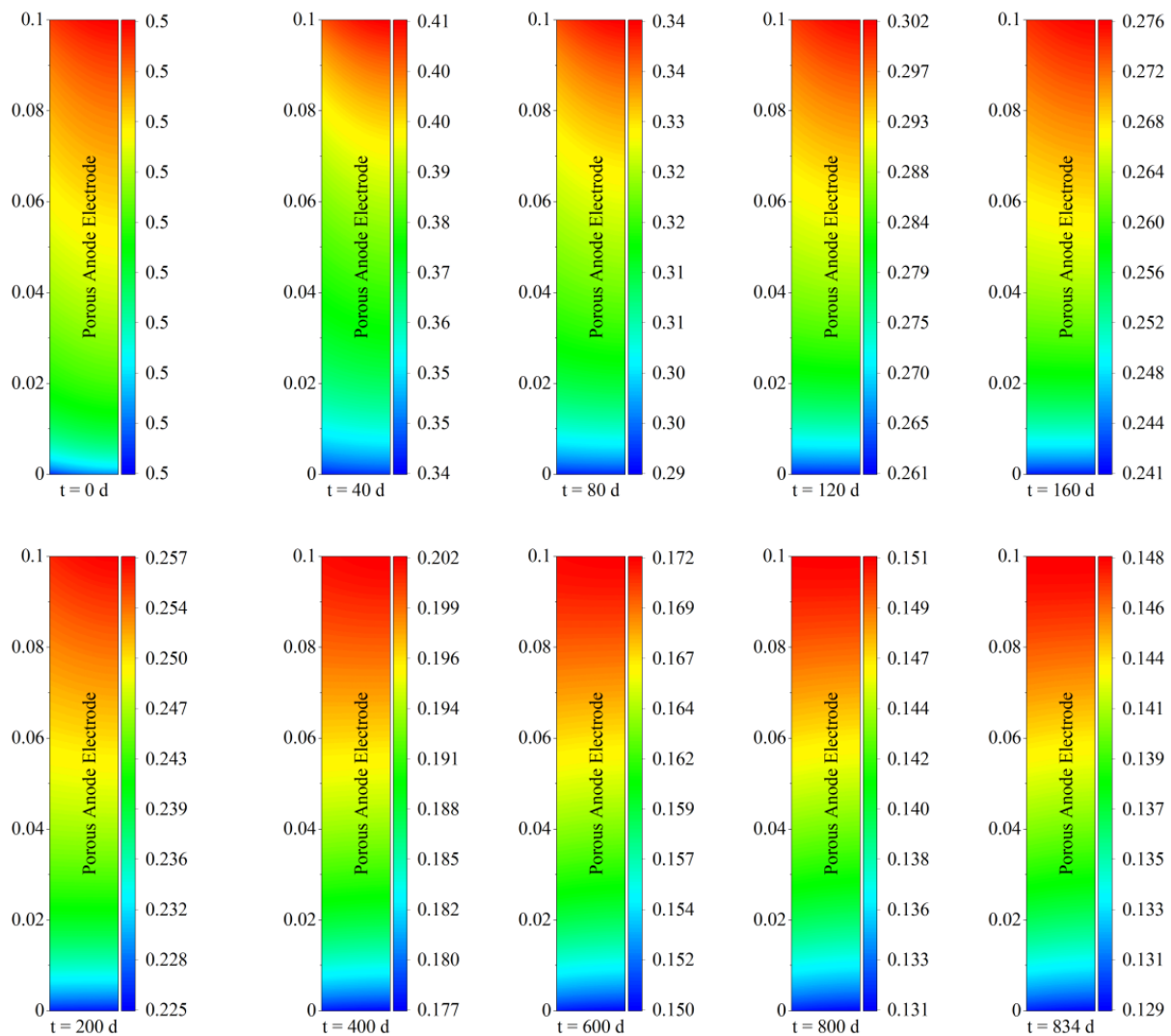
Figure 5. The spatial and temporal evolution of porosity within the porous anode electrode of the solid oxide fuel cell during 20,000 h of steady−state operation.

As shown in Figure 5, with regard to temporal evolution characteristics, the porosity of the porous electrode remained at the initial value of 0.5 because there was no obvious carbon deposition in the early stage of operation. As the operation time increased, the porous electrode porosity gradually decreased corresponding to the increase in deposited carbon shown in Figure 3. In terms of spatial maximum, the porosity of the porous electrode gradually decreased from 0.5 (0 days) to 0.41 (40 days), 0.34 (80 days), 0.3 (120 days), 0.276 (160 days), 0.257 (200 days), 0.202 (400 days), 0.172 (600 days), and 0.148 (834 days). With regard to spatial distribution characteristics, the porosity near the inlet of the porous electrode was lower than that near the outlet, and the porosity near the left fuel channel was also slightly lower than that near the right electrolyte. Taking the spatial distribution after operation for 40 days as an example, the porosity near the inlet of the porous electrode was 0.34, while that near the outlet was 0.41. The change in porosity was the direct result of carbon deposition. Therefore, it could be found that the spatial distribution of porosity was highly consistent with the carbon deposition shown in Figure 4. More specifically, taking the porosity of the porous electrode near the inlet side as an example, the original gas phase pores were heavily occupied by carbon deposition due to the higher deposited carbon concentration, causing a decrease in the proportion of gas transport channels, which was the direct cause of the decrease in porosity, while lower carbon deposition concentration induced a relatively higher porosity near the outlet.

In order to describe the variation trend of porous anode electrode porosity as varied by operating time more clearly, Figure 6 also demonstrates the detected values of local porosity at the electrode midpoint based on Figure 5. As shown in Figure 6, corresponding to the variation in carbon deposition, the local porosity also decreased rapidly at first and slowed down at later stages. In the early stages of operation, the local porosity remained at its initial value of 0.5 because there was no obvious carbon deposition. After the first 180 days of operation, the local porosity decreased rapidly to 0.26, almost half of the initial value. As the operation time increased from 180 days to 360 days, the local porosity decreased from 0.26 to 0.2, reaching a 23% decrease. A further decreased decline rate was found with the increase in operation time. Overall, the decrease in electrode porosity was concentrated in the first 4000 h of steady−state operation. These results also confirmed that key measures to inhibit carbon deposition within direct internal reforming solid oxide fuel cells can be placed in the early operation stage around 4000 h.
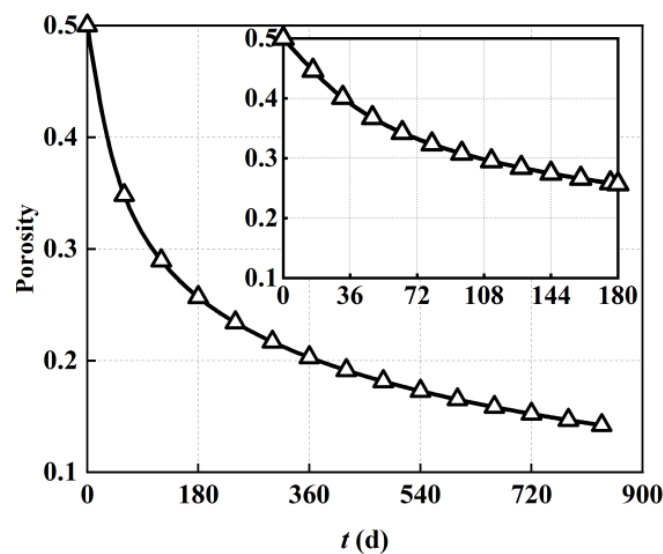
Figure 6. The variation in porous anode electrode porosity over operating time during 20,000 h of steady−state operation.

The void volume occupancy caused by carbon deposition within a porous electrode can deteriorate its transport properties. Therefore, taking permeability as the characteristic index, Figure 7 demonstrates the spatial and temporal evolution of permeability within the porous anode electrode of the solid oxide fuel cell caused by carbon deposition during 20,000 h of steady−state operation. As shown in Figure 7, with regard to temporal evolution characteristics, the permeability of the porous anode electrode decreased continually with the increase in operation time. More specifically, at the initial stage of operation, the porous electrode permeability remained at its initial value of 1.76×10^{-11} m^2. With the increase in operating time, the permeability of the porous electrode decreased rapidly, driven by the reduction in gas phase pore space. In terms of spatial maximum, the porous electrode permeability decreased from 1.76×10^{-11} m^2 (0 days) to 8.9×10^{-12} m^2 (40 days), 4.5×10^{-12} m^2 (80 days), 2.9×10^{-12} m^2 (120 days), 2.1×10^{-12} m^2 (160 days), 1.7×10^{-12} m^2 (200 days), 7.1×10^{-13} m^2 (400 days), 4×10^{-13} m^2 (600 days), 2.5×10^{-13} m^2 (800 days), and 2.3×10^{-13} m^2 (834 days). It could be found that the permeability of the porous electrode decreased by two orders of magnitude after 20,000 h of steady−state operation. It was inferred that the long-term performance degradation of the solid oxide fuel cell came not only from the decrease in reaction activity, but also from the deterioration of transport capacity.
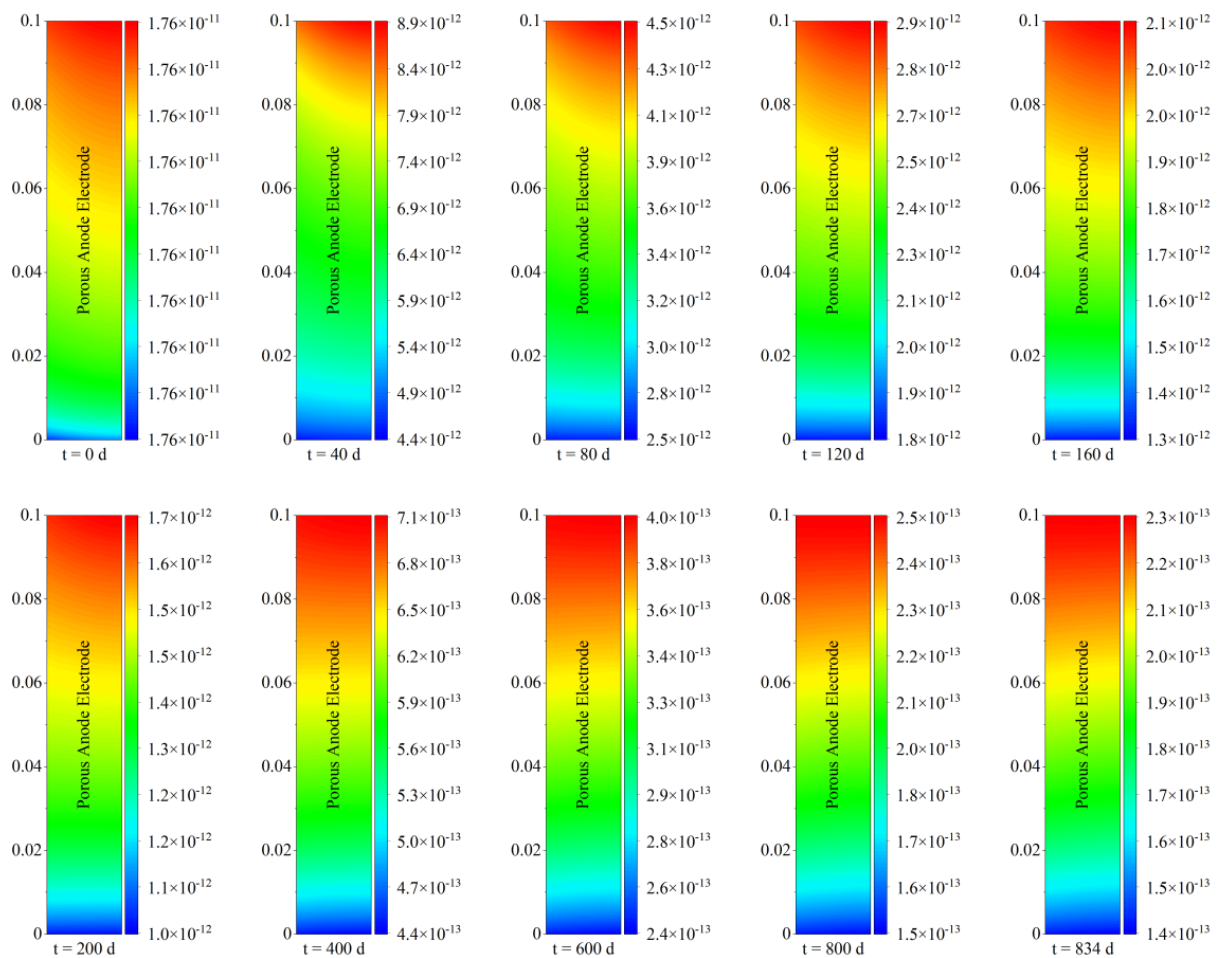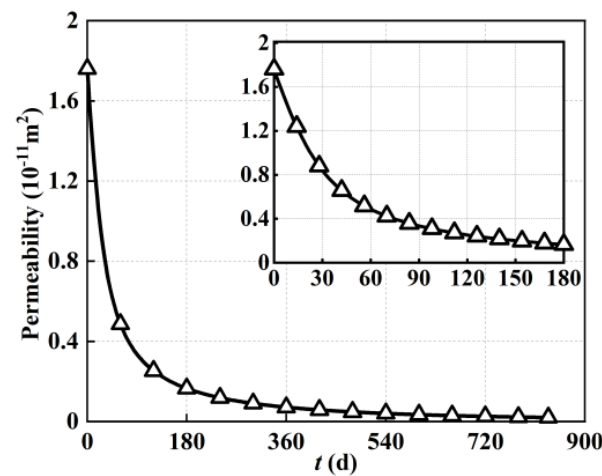
Figure 7. The spatial and temporal evolution of permeability (m^2) within the porous anode electrode of the solid oxide fuel cell during 20,000 h of steady−state operation.

With regard to spatial distribution characteristics, the deterioration of porous electrode permeability was consistent with its porosity. More specifically, the permeability near the inlet of the porous electrode was lower than that near the outlet, and the permeability of the porous electrode near the left fuel channel was also slightly lower than that near the right electrolyte. Taking the results after 40 days of operation as an example, the permeability near the inlet of the porous electrode was 4.4×10^{-12} m^2, while that near the outlet was 8.9×10^{-12} m^2. This meant that the permeability within the porous electrode also differed by half after 40 days of operation, which was similar to the increase in carbon deposition. This was because gas transport within the porous electrode occurred in the void volume. With the decrease in void volume within the porous electrode, the space for gas transport was reduced, directly resulting in a decrease in permeability. The correspondence between the doubling of carbon deposition and the halving of permeability indicated that the deposited carbon may remain in the same structure during this period.

In order to describe the variation trend of permeability within the porous anode electrode as varied by operating time more clearly, Figure 8 also demonstrates the detected values of local permeability at the electrode midpoint based on Figure 7. As shown in Figure 8, the decrease rate of permeability during the first 4000 h of steady−state operation far exceeded the decrease rate of porosity. The local permeability remained at its initial value of 1.76×10^{-11} m^2 at the early stage, while it rapidly decreased to 1.69×10^{-12} m^2 after 180 days of operation. In other words, the local permeability of the porous electrode decreased by one order of magnitude after 180 days of operation. Combined with the value of local permeability (1.87×10^{-13} m^2) after 20,000 h of steady−state operation, this means that the transport capacity deterioration of the porous electrode was concentrated in

the first 180 days of steady−state operation when fuel starvation of a solid oxide fuel cell may occur.

Figure 8. The variation in porous anode electrode permeability over the operating time during 20,000 h of steady−state operation.

4.3. The Effect of Carbon Deposition on Reaction Activity and Output Performance

As previously mentioned, deposited carbon adsorbs onto the solid surface of the porous electrode. The resulting coverage of the catalytic active site directly decreases the reaction activity within the porous electrode of a solid oxide fuel cell. To illustrate this effect, Figure 9 demonstrates the spatial and temporal evolution of the reaction activity within the porous anode electrode under varied operating time considering the carbon deposition effect. Before conducting the discussion, it should be noted that the reaction activity at the beginning of the operation was considered as the initial benchmark of 100%.

As can be seen from Figure 9, with regard to spatial distribution characteristics, the reaction activity near the inlet of the solid oxide fuel cell electrode was lower than that near the outlet, and the reaction activity near the left fuel channel was also lower than that near the right electrolyte. Taking the reaction activity condition after operation for 40 days as an example, the reaction activity near the porous electrode outlet was around 77%, while it was as low as 29% near the inlet. In other words, the reaction activity within the porous electrode was extremely uneven. After 40 days of steady−state operation, the reaction reactivity difference within the porous electrode was more than double. It could be inferred that the lower value of the reaction activity near the left inlet fuel channel was related to higher methane concentration and the resulting more severe carbon deposition. Similarly, on the opposite side, the higher hydrogen concentration and the lower methane concentration led to a relatively higher reactivity value.

With regard to temporal evolution characteristics, the reaction activity decreased continually with the increase in operation time during 20,000 h of steady−state operation. As shown in Figure 9, as the operating time increased, the reaction reactivity (spatial maximum) decayed rapidly from 100% (0 days) to 77% (40 days), 38% (80 day), 23% (120 days), 17% (160 days), 14% (200 days), 7.3% (400 days), 5.2% (600 days), 4.1% (800 days), and 4% (834 days). The reaction activity value was only 4% after 20,000 h of steady−state operation, which reflected the poor long-term performance of the direct internal reforming natural-gas-fueled solid oxide fuel cell.
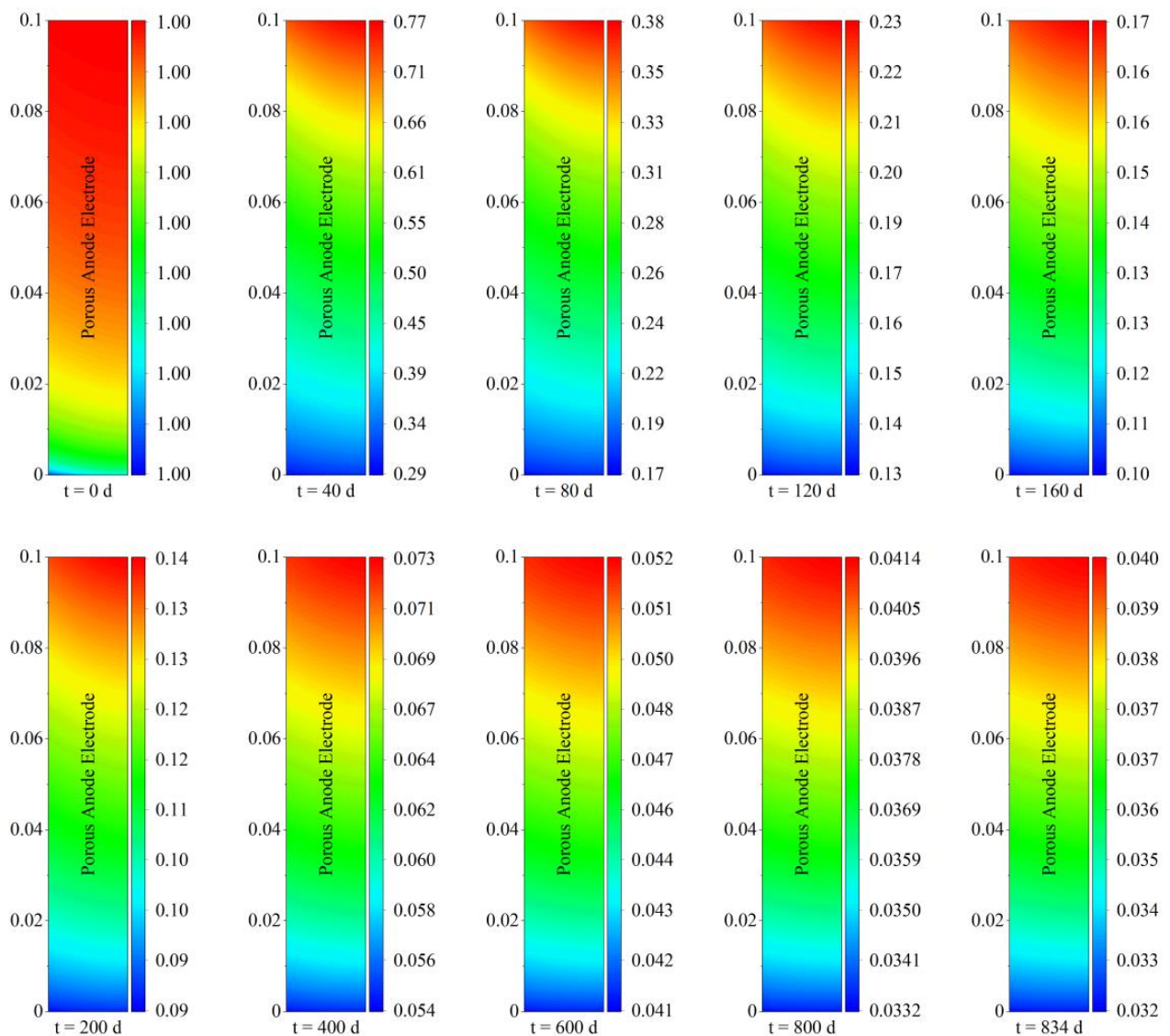
Figure 9. The spatial and temporal evolution of reaction activity within the porous anode electrode of the solid oxide fuel cell during 20,000 h of steady−state operation.

In order to describe the evolution trend of reaction activity under varied operating times more clearly, Figure 10 also demonstrates the detected values of local reaction activity at the electrode midpoint based on Figure 9. As shown in Figure 10, similar to the deterioration of permeability, the local reaction activity also experienced rapid decay during the first 4000 h of steady−state operation and slowed down at later stages. More specifically, the local reaction activity remained at its initial value of 100% at the early stage, while it rapidly decreased to 12.8% after 180 days of operation. As for the operation period from 180 days to 360 days, the reaction activity further decreased to 7.13%. The subsequent period of operation saw a slow decay from 7.13% (day 160) to a minimum of 3% (834 days). Overall, the decay was concentrated in the first 4000 h of steady−state operation, which also supported the judgement that early intervention is required to suppress carbon deposition.
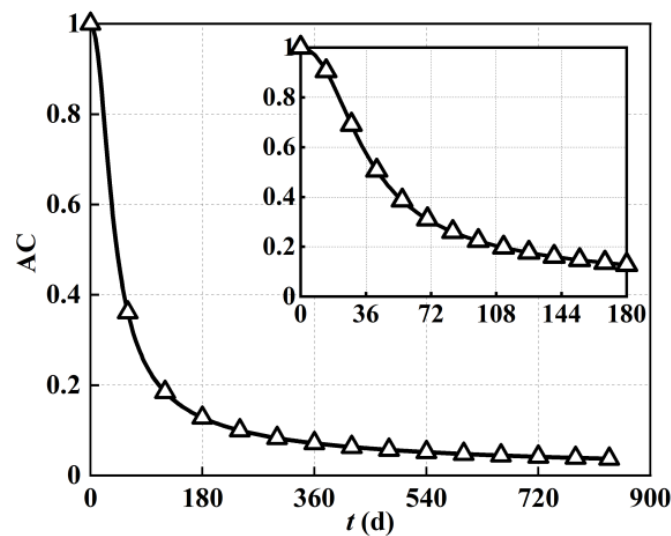
Figure 10. The variation in reaction activity within the porous anode electrode over operating time during 20,000 h of steady−state operation.

The combination of the decay of reaction activity and the deterioration of transport capacity within the porous electrode led to performance degradation of the solid oxide fuel cell. In order to elucidate the performance degradation of the solid oxide fuel cell caused by carbon deposition during long-term operation, Figure 11 demonstrates the spatial and temporal evolution of current density within the porous anode electrode of the solid oxide fuel cell during 20,000 h of steady−state operation.

As shown in Figure 11, with regard to spatial distribution characteristics, the current density near the inlet of the solid oxide fuel cell electrode was lower than that near the outlet, and the current density difference between the left fuel channel and the right electrolyte was not large. On one hand, the higher reaction reactivity and better fuel transport due to lower carbon deposition promoted a local electrochemical reaction near the outlet of the porous electrode. On the other hand, due to sufficient electrochemical reaction, a high local temperature was created by the release of heat from the electrochemical reaction, which in turn led to a further increase in current density. Taking the current density distribution after operation for 40 days as an example, the current density near the porous electrode outlet was around 4600 A/m^2, while it was as low as 400 A/m^2 near the inlet. This means that the current density distribution within the porous electrode was extremely uneven. Moreover, it is worth noting that, after 160 days of steady−state operation, a deactivation zone of 0 current density began to appear in the electrode inlet of the solid oxide fuel cell. Additionally, there was a tendency for the deactivation zone to gradually expand toward the outlet, which further deteriorated the output performance of the fuel cell. This indicates that the current density of the solid oxide fuel cell experienced a decrease of two orders of magnitude across the entire space, reflecting the poor long-term stability of the direct internal reforming natural-gas-fueled solid oxide fuel cell.

In order to directly illustrate the long-term performance degradation of the direct internal reforming solid oxide fuel cell, Figure 12 also demonstrates its variation in output current density during 20,000 h of steady−state operation. As shown in Figure 12, corresponding to the increase in carbon deposition, the output current density of the direct internal reforming solid oxide fuel cell deteriorated rapidly at first and slowed down at the later stage. More specifically, the output current density remained at the initial value of 3258 A/m^2 when the solid oxide fuel cell started operation because there was no obvious carbon deposition. Then, it rapidly decreased to 428 A/m^2 after 180 days (around 4000 h) of steady−state operation and further decreased to 67 A/m^2 after 20,000 h of operation. This means that the steady−state operation degradation rate of the solid oxide fuel cell for

180 days (around 4000 h) was relatively large, while the corresponding value for 834 days (around 20,000 h) was relatively small due to the lower output performance.
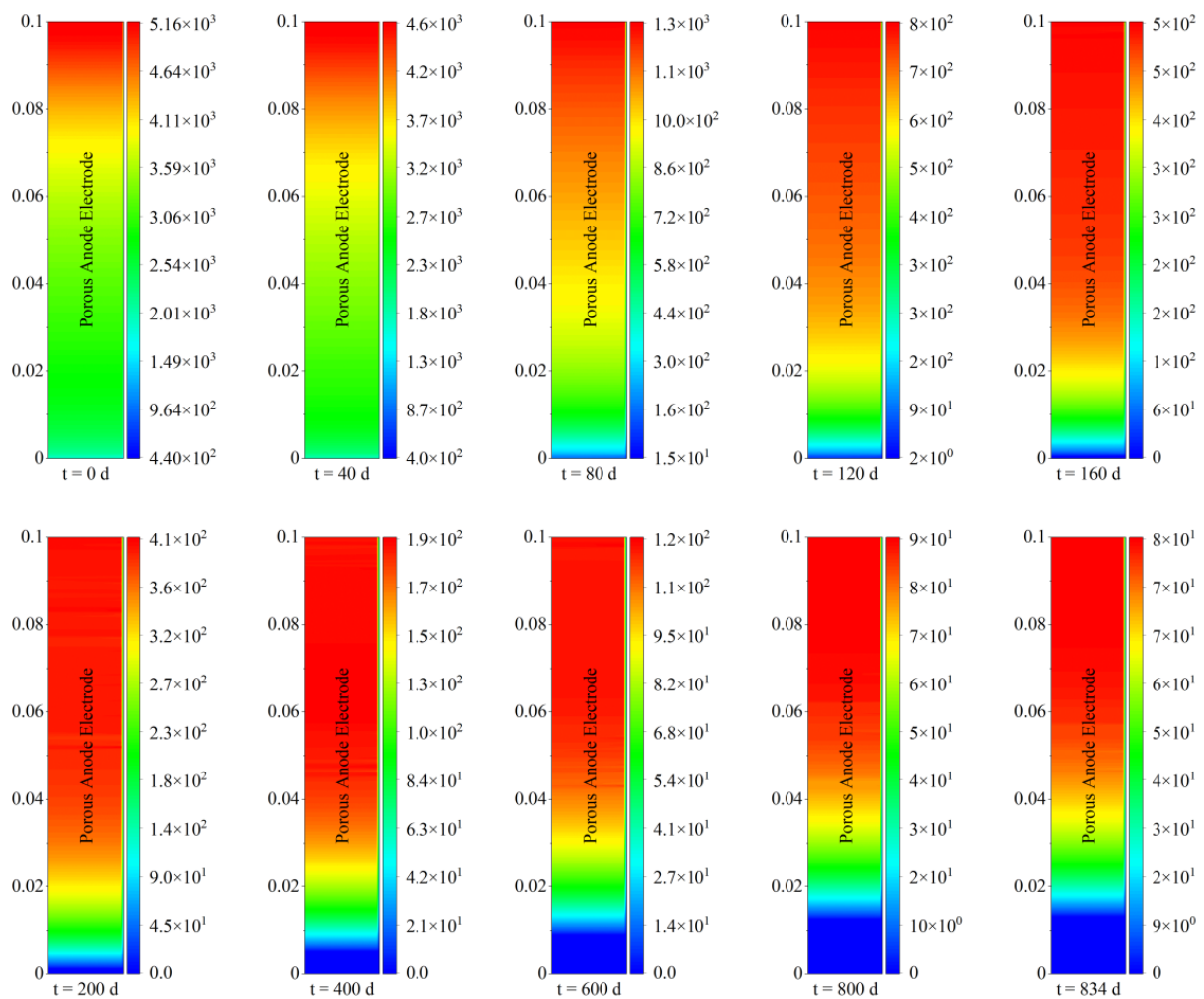
Figure 11. The spatial and temporal evolution of current density (A/m^2) within the porous anode electrode of the solid oxide fuel cell during 20,000 h of steady−state operation.
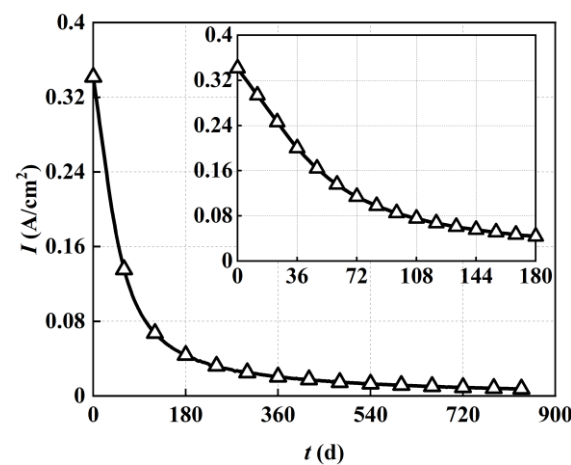
Figure 12. The variation in output current density of direct internal reforming solid oxide fuel cell during 20,000 h of steady−state operation.

The steady−state operation degradation rate of the solid oxide fuel cell for 180 days (around 4000 h) of operation in the present work was 20.1% per 1000 h, while the degradation rate was 4.9% per 1000 h for 834 days (around 20,000 h) of operation. In fact, the low current output after 4000 h of operation was not of engineering application value. The rapid performance degradation reflected the poor performance of the direct internal reforming solid oxide fuel cell, particularly with the appearance of the deactivation zone with 0 current density. Therefore, to avoid performance deterioration at the fuel inlet and maintain better long-term stability, we proposed an integrated system of a thermally self-sustained methane steam reformer and a solid oxide fuel cell in our previous work. The corresponding long-term performance degradation evaluation of this integrated system should also be conducted in future work.

5. Conclusions

To conduct the evaluation of long-term performance degradation caused by carbon deposition for a direct internal reforming natural-gas-fueled solid oxide fuel cell, a transient multi-physics numerical model coupled an electrochemical reaction and a thermochemical reaction; the transport of ions, electrons, heat, mass, and momentum; and the carbon deposition effect was developed. Then, the spatial and temporal evolution of carbon deposition within the solid oxide fuel cell during 834 days (around 20,000 h) of steady−state operation was elucidated for the first time, and the resulting effect on the output performance of the solid oxide fuel cell was clarified. The following main conclusions were drawn.

(1) Rapid development of carbon deposition was concentrated in the first 180 days (around 4000 h) of operation. The average growth rate of carbon deposition could reach 556 $mol/m^3/d$ during the first 180 days of operation, while it was only 194 $mol/m^3/d$ for 180–360 days of operation. Additionally, the deposited carbon concentration was extremely uneven within the porous electrode. The probe value of deposited carbon concentration near the outlet was around 29,000 mol/m^3, while it was as high as 59,000 mol/m^3 near the inlet. This indicated that key measures to inhibit carbon deposition should be implemented early in the first 180 days of operation and should focus on the anode inlet area of solid oxide fuel cells.

(2) Deposited carbon adsorbed onto the solid surface of the porous electrode and occupied its void volume, causing decreases in porous electrode porosity and permeability. In addition, the rapid deceases in local porosity and permeability were also concentrated in the first 180 days (around 4000 h) of operation. The probe value of local porosity decreased rapidly from 0.5 to 0.26, with a decrease rate of almost half during the first 180 days of operation, while it decreases from 0.26 to 0.2, with a decrease of 23% from 180 to 360 days of operation. Accordingly, the permeability of the porous electrode near the inlet decreased by two orders of magnitude after 20,000 h of steady−state operation. It was inferred that changes in the porous electrode microscopic morphology and the resulting deterioration of transport properties could significantly affect the long-term performance of a solid oxide fuel cell by inducing fuel starvation.

(3) Coverage of the catalytic active site caused by deposited carbon decayed the reaction activity and led to the output performance degradation of the solid oxide fuel cell. The corresponding deterioration of output current density was also concentrated in the first 180 days operation. The output current density remained at 3258 A/m^2 when the solid oxide fuel cell started operation, but it rapidly decreased to 428 A/m^2 after 180 days of operation. Moreover, it is worth noting that, after 160 days of operation, a deactivation zone with 0 current density began to appear in the electrode inlet of the solid oxide fuel cell. Additionally, there was a tendency for the deactivation zone to gradually expand toward the outlet, which further deteriorated the output performance of the fuel cell. The performance degradation reflected the poor long-term stability of the direct internal reforming natural-gas-fueled solid oxide fuel cell and the necessity of the pre-reformed operation of natural gas through the integrated

system of a thermally self-sustained methane steam reformer and a solid oxide fuel cell proposed in our previous work.

Institutional Review Board Statement: The study did not require ethical approval.

Informed Consent Statement: The study did not involve humans.

Data Availability Statement: To ensure the rigor and repeatability of the study, the authors can provide source data and model procedures related to this study upon reasonable request.

Conflicts of Interest: The authors declare that they have no known competing financial interests or personal relationships that could have appeared to influence the work reported in this paper.

References

1. Joung, T.; Kang, S.; Lee, J.; Ahn, J. The IMO initial strategy for reducing Greenhouse Gas (GHG) emissions, and its follow-up actions towards 2050. *J. Int. Marit. Saf. Environ. Aff. Shipp.* **2020**, *4*, 1–7. [CrossRef]
2. Sapra, H.; Stam, J.; Reurings, J.; van Biert, L.; van Sluijs, W.; de Vos, P.; Visser, K.; Vellayani, A.P.; Hopman, H. Integration of solid oxide fuel cell and internal combustion engine for maritime applications. *Appl. Energy* **2021**, *281*, 115854. [CrossRef]
3. Boldrin, P.; Brandon, N. Progress and outlook for solid oxide fuel cells for transportation applications. *Nat. Catal.* **2019**, *2*, 571–577. [CrossRef]
4. Papaefthimiou, V.; Shishkin, M.; Niakolas, D.K.; Athanasiou, M.; Law, Y.T.; Arrigo, R.; Teschner, D.; Hävecker, M.; Knop-Gericke, A.; Schlögl, R. On the active surface state of nickel-ceria solid oxide fuel cell anodes during methane electrooxidation. *Adv. Energy Mater.* **2013**, *3*, 762–769. [CrossRef]
5. Hua, B.; Li, M.; Sun, Y.-F.; Zhang, Y.-Q.; Yan, N.; Li, J.; Etsell, T.; Sarkar, P.; Luo, J.-L. Grafting doped manganite into nickel anode enables efficient and durable energy conversions in biogas solid oxide fuel cells. *Appl. Catal. B Environ.* **2017**, *200*, 174–181. [CrossRef]
6. Neagu, D.; Papaioannou, E.I.; Ramli, W.K.W.; Miller, D.N.; Murdoch, B.J.; Ménard, H.; Umar, A.; Barlow, A.J.; Cumpson, P.J.; Irvine, J.T.S. Demonstration of chemistry at a point through restructuring and catalytic activation at anchored nanoparticles. *Nat. Commun.* **2017**, *8*, 1855. [CrossRef]
7. Li, X.; Liu, M.; Lai, S.Y.; Ding, D.; Gong, M.; Lee, J.-P.; Blinn, K.S.; Bu, Y.; Wang, Z.; Bottomley, L.A. In situ probing of the mechanisms of coking resistance on catalyst-modified anodes for solid oxide fuel cells. *Chem. Mater.* **2015**, *27*, 822–828. [CrossRef]
8. Rabuni, M.; Li, T.; Punmeechao, P.; Li, K. Electrode design for direct-methane micro-tubular solid oxide fuel cell (MT-SOFC). *J. Power Sources* **2018**, *384*, 287–294. [CrossRef]
9. Zhao, K.; Hou, X.; Bkour, Q.; Norton, M.; Ha, S. NiMo-ceria-zirconia catalytic reforming layer for solid oxide fuel cells running on a gasoline surrogate. *Appl. Catal. B Environ.* **2018**, *224*, 500–507. [CrossRef]
10. Zhang, T.; Liu, Z.; Zhu, Y.; Liu, Z.; Sui, Z.; Zhu, K.; Zhou, X. Dry reforming of methane on Ni-Fe-MgO catalysts: Influence of Fe on carbon-resistant property and kinetics. *Appl. Catal. B Environ.* **2020**, *264*, 118497. [CrossRef]
11. Zhai, S.; Xie, H.; Chen, B.; Ni, M. A rational design of FeNi alloy nanoparticles and carbonate-decorated perovskite as a highly active and coke-resistant anode for solid oxide fuel cells. *Chem. Eng. J.* **2022**, *430*, 132615. [CrossRef]
12. Sarruf, B.; Hong, J.; Steinberger-Wilckens, R.; de Miranda, P. CeO$_2$Co$_3$O$_4$CuO anode for direct utilisation of methane or ethanol in solid oxide fuel cells. *Int. J. Hydrogen Energy* **2018**, *43*, 6340–6351. [CrossRef]
13. Kim, S.; Kim, C.; Lee, J.H.; Shin, J.; Lim, T.; Kim, G. Tailoring Ni-based catalyst by alloying with transition metals (M = Ni, Co, Cu, and Fe) for direct hydrocarbon utilization of energy conversion devices. *Electrochim. Acta* **2017**, *225*, 399–406. [CrossRef]
14. Shishkin, M.; Ziegler, T. Direct modeling of the electrochemistry in the three-phase boundary of solid oxide fuel cell anodes by density functional theory: A critical overview. *Phys. Chem. Chem. Phys.* **2014**, *16*, 1798–1808. [CrossRef] [PubMed]
15. Qu, J.; Wang, W.; Chen, Y.; Deng, X.; Shao, Z. Stable direct-methane solid oxide fuel cells with calcium-oxide-modified nickel-based anodes operating at reduced temperatures. *Appl. Energy* **2016**, *164*, 563–571. [CrossRef]
16. Kirtley, J.; Singh, A.; Halat, D.; Oswell, T.; Hill, J.; Walker, R. In Situ Raman Studies of Carbon Removal from High Temperature Ni–YSZ Cermet Anodes by Gas Phase Reforming Agents. *J. Phys. Chem. C* **2013**, *117*, 25908–25916. [CrossRef]
17. Schluckner, C.; Subotić, V.; Lawlor, V.; Hochenauer, C. Carbon Deposition Simulation in Porous SOFC Anodes: A Detailed Numerical Analysis of Major Carbon Precursors. *J. Fuel Cell Sci. Technol.* **2015**, *12*, 051007. [CrossRef]

18. Takenaka, S.; Kato, E.; Tomikubo, Y.; Otsuka, K. Structural change of Ni species during the methane decomposition and the subsequent gasification of deposited carbon with CO_2 over supported Ni catalysts. *J. Catal.* **2003**, *219*, 176–185. [CrossRef]

19. Snoeck, J.; Froment, G.; Fowles, M. Steam/CO_2 Reforming of Methane. Carbon Filament Formation by the Boudouard Reaction and Gasification by CO_2, by H_2, and by Steam: Kinetic Study. *Ind. Eng. Chem. Res.* **2002**, *41*, 4252–4265. [CrossRef]

20. Subotić, V.; Schluckner, C.; Mathe, J.; Rechberger, J.; Schroettner, H.; Hochenauer, C. Anode regeneration following carbon depositions in an industrial-sized anode supported solid oxide fuel cell operating on synthetic diesel reformate. *J. Power Sources* **2015**, *295*, 55–66. [CrossRef]

21. Subotić, V.; Schluckner, C.; Stoeckl, B.; Preininger, M.; Lawlor, V.; Pofahl, S.; Schroettner, H.; Hochenauer, C. Towards practicable methods for carbon removal from Ni-YSZ anodes and restoring the performance of commercial-sized ASC-SOFCs after carbon deposition induced degradation. *Energy Convers. Manag.* **2018**, *178*, 343–354. [CrossRef]

22. Han, Z.; Yang, Z.; Han, M. Cell-protecting regeneration from anode carbon deposition using in situ produced oxygen and steam: A combined experimental and theoretical study. *J. Mater. Sci. Technol.* **2018**, *34*, 2375–2383. [CrossRef]

23. Yan, M.; Zeng, M.; Chen, Q.; Wang, Q. Numerical study on carbon deposition of SOFC with unsteady state variation of porosity. *Appl. Energy* **2012**, *97*, 754–762. [CrossRef]

24. Ma, T.; Yan, M.; Zeng, M.; Yuan, J.; Chen, Q.; Sundén, B.; Wang, Q. Parameter study of transient carbon deposition effect on the performance of a planar solid oxide fuel cell. *Appl. Energy* **2015**, *152*, 217–228. [CrossRef]

25. Zhang, K.; Wang, S.; Li, B.; He, Y. Performance of solid oxide fuel cell with chemical looping gasification products as fuel. *Int. J. Hydrogen Energy* **2021**, *46*, 30135–30144. [CrossRef]

26. Zhu, P.; Yao, J.; Wu, Z.; Huang, S.; Radzi Abu Mansor, M.; Yang, F.; Zhang, Z. Construction of a transient multi-physics model of solid oxide fuel cell fed by biomass syngas considering the carbon deposition and temperature effect. *Chem. Eng. J.* **2022**, *442*, 136159. [CrossRef]

27. Li, A.; Song, C.; Lin, Z. A multiphysics fully coupled modeling tool for the design and operation analysis of planar solid oxide fuel cell stacks. *Appl. Energy* **2017**, *190*, 1234–1244. [CrossRef]

28. Fang, X.; Zhu, J.; Lin, Z. Effects of electrode composition and thickness on the mechanical performance of a solid oxide fuel cell. *Energies* **2018**, *11*, 1735. [CrossRef]

29. Guo, M.; Ru, X.; Lin, Z.; Xiao, G.; Wang, J. Optimization design of rib width and performance analysis of solid oxide electrolysis cell. *Energies* **2020**, *13*, 5468. [CrossRef]

30. Li, Z.; Yang, G.; Cui, D.; Li, S.; Shen, Q.; Zhang, G.; Zhang, H. Modeling and evaluating of thermo-electro-chemo-mechanical behavior for pre-reformed methane-fueled solid oxide fuel cell. *J. Power Sources* **2022**, *522*, 230981. [CrossRef]

31. Zavarukhin, S.; Kuvshinov, G. The kinetic model of formation of nanofibrous carbon from CH4–H2 mixture over a high-loaded nickel catalyst with consideration for the catalyst deactivation. *Appl. Catal. A Gen.* **2004**, *272*, 219–227. [CrossRef]

32. Singhal, S.; Kendall, K. *High-Temperature Solid Oxide Fuel Cells: Fundamentals, Design and Applications*; Elsevier: Amsterdam, The Netherlands, 2003. [CrossRef]

33. van Biert, L.; Visser, K.; Aravind, P. A comparison of steam reforming concepts in solid oxide fuel cell systems. *Appl. Energy* **2020**, *264*, 114748. [CrossRef]

34. Hsieh, Y.D.; Chan, Y.H.; Shy, S.S. Effects of pressurization and temperature on power generating characteristics and impedances of anode-supported and electrolyte-supported planar solid oxide fuel cells. *J. Power Sources* **2015**, *299*, 1–10. [CrossRef]

35. Yurkiv, V. Reformate-operated SOFC anode performance and degradation considering solid carbon formation: A modeling and simulation study. *Electrochim. Acta* **2014**, *143*, 114–128. [CrossRef]